Mühendis ve Makina / Engineer and Machinery
https://dergipark.org.tr/tr/pub/muhendismakina

FLUID-STRUCTURE INTERACTION-BASED NUMERICAL SIMULATION OF ELASTIC DEFORMATION ON A CANTILEVER BEAM WITH INFINITE ASPECT RATIO

Hüseyin Can Önel [1]*

1 Adana Science and Technology University, Faculty of Aeronautics and Astronautics, Department of Aerospace Engineering, Adana, Turkey

ORCID No: http://orcid.org/0000-0002-4055-7706

Anahtar Kelimeler

aeroelasticity, fluid-structure interaction, turbulent flows, computational fluid dynamics, finite volume method

Öz

In this study, the deformation of a 2D flat plate with varying angles of attack is numerically examined, focusing on the impact of structural deformation on aerodynamic performance. Traditionally, aerodynamic analyses assume rigid body behavior, but in this case, the effects of elasticity are considered through a coupled fluid-structure interaction (FSI) approach. Both the fluid and solid domains are solved using OpenFOAM, a finite volume-based solver. The fluid flow is modeled as turbulent, and the structure's elastic deformation is incorporated into the analysis. Initially, uncoupled simulations are validated against experimental and analytical reference cases. Following this, a coupled simulation is conducted, where deformations and changes in aerodynamic coefficients are compared to rigid-body assumptions. The results show good agreement with reference data for uncoupled cases. However, in the coupled simulations, significant deviations in aerodynamic performance are observed due to the structural deformation. Specifically, for the elastic plate, lift coefficient losses of up to 6% and drag coefficient increases of up to 47% are observed compared to the rigid-body assumption. This study demonstrates the importance of accounting for aeroelastic effects in simulations involving flexible structures, as neglecting structural elasticity can lead to significant inaccuracies in aerodynamic predictions.

* hconel@atu.edu.tr

doi: 10.46399/muhendismakina.1707666

SONSUZ KANAT AÇIKLIĞINA SAHİP BİR KONSOL KİRİŞİN AKIŞKAN-YAPI ETKİLEŞİMİ KAYNAKLI ELASTİK DEFORMASYONUNUN SAYISAL SİMÜLASYONU

Keywords

aeroelastisite, akışkan-yapı etkileşimi, türbülanslı akış, hesaplamalı akışkanlar dinamiği, sonlu hacim metodu

Abstract

Bu çalışmada, değişen hücum açılarındaki 2 boyutlu düz bir levhanın deformasyonu sayısal olarak incelenmiş ve yapısal deformasyonun aerodinamik performans üzerindeki etkilerine odaklanılmıştır. Geleneksel olarak, aerodinamik analizlerde yapı rijit kabul edilir; ancak bu çalışmada esneklik etkileri, akışkan-yapı etkileşimi (FSI) yaklaşımı ile dikkate alınmıştır. Hem akışkan hem de katı bölgeler, sonlu hacimler yöntemine dayalı OpenFOAM yazılımı kullanılarak çözülmüştür. Akışkan alan türbülanslı olarak modellenmiş, yapının elastik deformasyonu çözüme dahil edilmiştir. İlk olarak, bağlaşık olmayan (uncoupled) simülasyonlar deneysel ve analitik referanslarla doğrulanmıştır. Daha sonra, bağlaşık (coupled) bir simülasyon gerçekleştirilmiş; elde edilen deformasyonlar ve aerodinamik katsayı değişimleri, rijit gövde varsayımıyla karşılaştırılmıştır. Bağlaşık olmayan simülasyonlar referans verilerle iyi uyum göstermiştir. Ancak bağlaşık çözümde, yapısal deformasyonun aerodinamik performansta belirgin sapmalara neden olduğu görülmüştür. Özellikle elastik levhada, rijit gövdeye kıyasla taşıma katsayısında %6'ya varan kayıplar, sürükleme katsayısında ise %47'ye varan artışlar gözlemlenmiştir. Bu çalışma, esnek yapıların yer aldığı simülasyonlarda aeroelastik etkilerin hesaba katılmasının önemini ve yapısal elastisitenin ihmal edilmesinin aerodinamik tahminlerde ciddi hatalara yol açabileceğini ortaya koymaktadır.

Araştırma Makalesi			Research Article		
Başvuru Tarihi	:	27.05.2025	Submission Date	:	27.05.2025
Kabul Tarihi	:	14.07.2025	Accepted Date	:	14.07.2025

1. Introduction and Background

Fluid-structure interaction (FSI) is a complex physical process of mutual influence between aerodynamic loads and structural deformations, which plays a crucial role in aerospace and engineering applications. Such interactions, especially for highly flexible structures, can lead to aerodynamic instabilities and limit cycle oscillations (LCO). Traditional aerodynamic analyses often assume rigid bodies, but recent studies show that structural deformations can significantly alter aerodynamic loads, making FSI models indispensable for aeroelastic simulations. In this context, high-precision FSI solutions are helping to better understand fundamental aerodynamic events and provide more reliable predictions in engineering designs.

Three distinct numerical simulation methods emerge for aeroelasticity and fluid-structure interaction. Low-fidelity techniques use simple, computationally efficient approaches such as the Unsteady Vortex Lattice Method and Blade Element Momentum theory. For instance, (Maza, Preidikman & Flores, 2023) and (Grinderslev, González Horcas & Sørensen, 2021) report that these methods suit linear or weakly nonlinear problems. Medium-fidelity methods incorporate some nonlinearities and unsteady effects with moderate computational expense; studies such as (Piperno, 1997), (Silva & Bartels, 2002), and (Chimakurthi, Tang, Palacios, Cesnik & Shyy, 2008) employ staggered Euler equations, reduced-order CFD models, and partitioned coupling strategies to capture more complex phenomena. High-fidelity approaches combine full computational fluid dynamics (via ALE, Navier-Stokes, or related formulations) with detailed structural models using FEM or multi-body methods. (Geuzaine, Brown, Harris & Farhat, 2003), (Grifò, Da Ronch & Benedetti, 2023), and (Heinz, Sørensen & Zahle, 2016) demonstrate that these methods resolve nonlinearities, large deformations, and unsteady flow effects, despite their higher computational cost. For a comprehensive review of these techniques, see (Schuster, Liu & Huttsell, 2003).

A review of previous studies reveals various approaches to aeroelastic analysis. (Neumann, Nitzsche & Voss, 2008) developed a bidirectional partitioned FSI coupling method that combines the Computational Fluid Dynamics (CFD) code of Deutsches Zentrum für Luft- und Raumfahrt (DLR), TAU, with MSC.NASTRAN for structural analysis. This method accounts for nonlinear aerodynamic effects and has been applied to both stable and unstable aeroelastic analyses, validated by wind tunnel experiments with good agreement. (Fagley, Seidel & McLaughlin, 2015) created a fully coupled aeroelastic model to examine dynamic instabilities like stall and flutter in a NACA 0018 airfoil. They used the HPCMP CREATETM-AV Kestrel software to compare wing structures at various stiffness levels. The results demonstrated how pressure gradients in the spanwise direction influence aerodynamic deformations and flow separation structures on the wing. Ayaz and Memon (Ayaz & Memon, 2022) analyzed the aeroelastic response of a flat plate using a bidirectional FSI coupling in both the frequency and time domains. Their simulations, using ANSYS software, incorporated dynamic mesh motion and CFL-based time stepping strategies. Their results showed that, compared to rigid body assumptions, considering viscous flow and elasticity provided more accurate predictions of important fluid-structure interactions such as limit cycle oscillations and flutter. (Badshah, Badshah & Jan, 2020) compared the performance of FSI models with rigid body models, noting that FSI models provide more realistic predictions by incorporating deformation effects in rotor blades. However, deformation did not significantly alter the separation characteristics. Still, the calculated power coefficients matched experimental data within a 10% error margin. (Sheta, Harrand, Thompson & Strganac, 2002) showed that FSI models can capture limit cycle oscillations in nonlinear aeroelastic systems, although details on validation error metrics were

not provided. Similarly, (Wood, Breuer & De Nayer, 2020) presented experimental data for a two-degree-of-freedom wing at low Reynolds numbers, reporting fluid-structure interactions that rigid body models could not capture. (Nawafleh, Xing, Durgesh & Padilla, 2022) studied the limit cycle oscillations of a flapping flag using a bidirectional coupled FSI model in ANSYS, finding error margins ranging from 0.7% to 6.41% in predictions of oscillation amplitude, drag coefficient, and frequency. This study also revealed important dynamic phenomena, including flow separation and negative drag.

The literature review indicates that FSI provides more accurate predictions and can account for various aerodynamic phenomena compared to traditional rigid body models. However, most studies focus on the aeroelastic behavior of airfoil profiles or three-dimensional structures and have not sufficiently addressed the detailed analysis of simple geometries like flat plates. Flat plates, however, are critical for understanding fundamental fluid-structure interaction mechanisms, making accurate numerical simulations essential.

1.1 Aim and Approach

This study will analyze the fluid-structure interaction of a two-dimensional flexible plate, exploring the limitations of rigid body assumptions and the role of nonlinear aeroelastic effects in the flow field. FSI solutions will be compared with traditional rigid models to investigate changes in dynamic flow structures on the plate's surface. Additionally, the accuracy of limit cycle oscillation frequency and amplitude predictions from coupled aeroelastic solutions will be assessed. The simulations are expected to contribute to understanding the behavior of flexible plates under flow effects.

2. Method

The study is entirely conducted through numerical methods. The aeroelastic solutions are primarily based on two solvers: a flow solver and a solid solver. Another key element of the method is the interface that ensures the coupling (interaction) between these two solvers. For both solutions (flow and solid), OpenFOAM, an open-source solver, was used (Weller, Tabor, Jasak & Fureby, 1998). OpenFOAM, which is essentially a partial differential equation system solver, is a widely used program based on the finite volume method. It offers various numerical schemes, solution mesh tools, and solution control methods, and allows for modifications to the existing code or the addition of new codes. It is commonly used for both academic and commercial purposes.

This study complied with research and publication ethics.

2.1 Equations Solved

In the turbulent fluid simulations, the full Reynolds-Averaged Navier-Stokes equations were solved in a time-dependent manner (URANS) in a two-dimensional domain with the assumption of incompressible fluid flow.

$$\frac{\partial U_i}{\partial x_i} = 0 \qquad \text{Eq. 1}$$

$$\frac{DU_i}{Dt} = -\frac{1}{\rho_f}\frac{\partial p}{\partial x_i} + \frac{\partial}{\partial x_j}(2\nu_f S_{ji} - \overline{u'_j u'_i}) \qquad \text{Eq. 2}$$

$$S_{ij} = \frac{1}{2}\left(\frac{\partial U_i}{\partial x_j} + \frac{\partial U_j}{\partial x_i}\right) \quad \text{Eq. 3}$$

Here, Eq. 1 and Eq. 2 represent the mass conservation and linear momentum conservation, respectively. The symbols are defined as follows: U_i is the velocity vector, p is the static pressure, x_i is the spatial coordinate vector, ρ_f is the fluid density, and ν_f is the kinematic viscosity of the fluid. The "material derivative" operator is defined as $\frac{D}{Dt} = \frac{\partial}{\partial t} + U_i \frac{\partial}{\partial x_i}$ (where t is the temporal dimension), and S_{ij} is the strain rate tensor. u'_i represents the turbulent velocity fluctuations. The term $\overline{u'_j u'_i}$, the time-averaged cross product of the velocity fluctuations, is referred to as the Reynolds stress tensor and requires turbulence modeling. In this study, the $k-\omega-SST$ turbulence model (Menter, Kuntz & Langtry, 2003) was used. An important turbulence parameter, turbulent kinetic energy, is defined as $k = \frac{1}{2}\overline{u'_j u'_i}$. This turbulence model switches to the $k-\omega$ model in regions of high viscosity (especially near walls), solving for the specific dissipation rate of the turbulent kinetic energy, ω. In regions far from walls, the model transitions to the $k-\epsilon$ model, solving for the dissipation rate of the turbulent kinetic energy, ϵ. By combining the strengths of both models, high-accuracy turbulent flow solutions are achieved. A mesh with wall-normal grid spacing satisfying the $y^+ \approx 1$ condition was used to achieve a fully resolved boundary layer flow. The velocity-pressure decoupling problem in incompressible flows was solved using the PIMPLE algorithm, which combines the SIMPLE (Issa, 1986) and PISO (Patankar & Spalding, 1983) algorithms, with the `OpenFOAM` solver `pimpleFoam`. Due to the nature of the problem, numerical solutions were obtained iteratively, with a convergence criterion of tolerance set to 10^{-6} for all linear system solutions, time steps, and iterations. Second-order accurate integration schemes for divergence and gradient in space and time were applied. For more detailed information on the turbulence model and algorithms, the referenced works should be consulted.

The equation representing the time-dependent deformations and stresses in the solid body is given in Eq. 4.

$$\rho_s \frac{\partial^2 w_i}{\partial t^2} = \frac{\partial}{\partial x_j}\left[\lambda \frac{\partial w_k}{\partial x_k}\delta_{ij} + \mu_s\left(\frac{\partial w_i}{\partial x_j} + \frac{\partial w_j}{\partial x_i}\right)\right] \quad \text{Eq. 4}$$

The left-hand side of the equation represents the inertial forces. ρ_s is the solid density, w_i is the displacement vector, λ is the first parameter associated with Lamé's bulk modulus, δ_{ij} is the Kronecker delta (which contributes only to the diagonal stress components), and μ_s the shear modulus (the second parameter of Lamé). These equations, solved simultaneously for the x (x_1) and y (x_2) coordinates in two-dimensional space, describe the balance of internal forces and inertial effects due to deformation, representing the propagation of displacements and stresses in a linear elastic solid. The solidDisplacementFoam solver in OpenFOAM was used for solving this equation. The solid was assumed to have linear elasticity.

2.2 Solution Grids

The total solution domain in the simulations consists of a two-dimensional circular flow region with a plate placed at the center. Both the fluid and solid domains were discretized using the finite volume method. The fluid domain has a hybrid mesh consisting of quadrilateral and triangular cells, while the solid domain is composed of a fully quadrilateral,

orthogonal, structured mesh (Figure 1). To ensure accurate and efficient deformation of the solution grid in the flow field around the solid, the cells near the solid were refined, allowing the cells to gradually grow larger as they approach the free-stream boundary. The current configuration of the flow region consists of 23000 cells, and the solid region consists of 1800 cells. This low number of cells was achieved thanks to the absence of wake refinement.

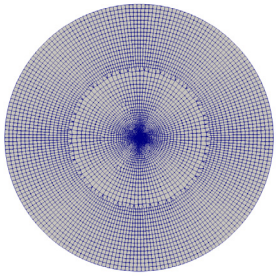

(a) Complete view of the computational grid

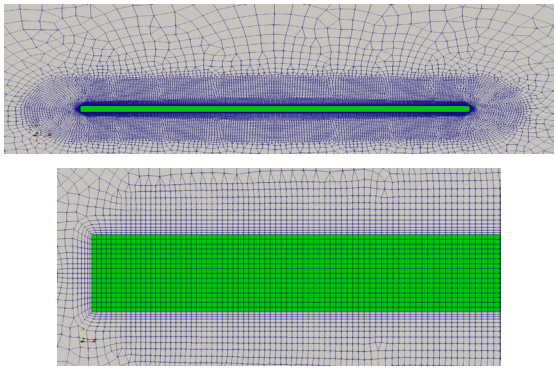

(b) Top: Detailed view of the plate (solid mesh hidden). Bottom: Close-up views of the fluid (gray) and solid (green) meshes

Figure 1: Solution grids used in the simulations

For the fluid domain, free-stream boundary conditions were applied at the farfield boundary, while a zero pressure gradient and zero velocity conditions were applied at the wall. Additionally, a zero turbulence kinetic energy boundary condition was applied at the wall. By setting the first cell height at the wall 0.1 mm, a non-dimensional wall distance of $y^+ \approx 1$ was achieved ensuring a fully resolved boundary layer solution without the need for wall functions. In the aeroelastic simulations, the plate was fixed at the trailing edge (with a zero displacement boundary condition), while free movement was allowed for the other surfaces (bottom, top, and leading edge). To balance the computational load and time between the fluid and solid solutions, the fluid solutions were computed in parallel on 2 processor cores, while the solid solutions were computed serially on a single core.

2.3 The Fluid-Structure Coupling and the Aeroelastic Model

The fluid and solid solvers of OpenFOAM were coupled through the preCICE adapter framework (Chourdakis, Davis, Rodenberg, Schulte, Simonis, Uekermann, Abrams, Bungartz, Cheung Yau, Desai, Eder, Hertrich, Lindner, Rusch, Sashko, Schneider, Totounferoush, Vol-

land, Vollmer & Koseomur, 2022) (Chourdakis, Schneider & Uekermann, 2023). Both solvers were executed simultaneously and in parallel with each other. During each time step, data such as pressure distribution and displacement were exchanged between the fluid and solid solvers. Since these data influence each other, iterations were performed within each time step until full convergence was achieved, and the convergence was monitored. Thus, there is a complete implicit (strong) coupling between the fluid and solid solvers. To obtain accurate solutions, the time step was kept at around .

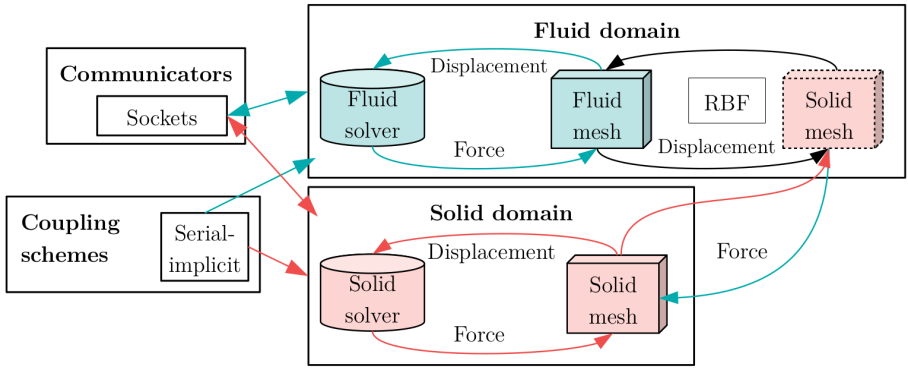

Figure 2: Diagram of the fluid-solid coupling

In a single time step, the flow field is first calculated with the current geometry. The pressure distribution data obtained on the solid surface are passed to the solid solver, and the displacement of each cell edge on the surface is computed (Figure 2). This displacement information is then passed back to the flow solver, which deforms the mesh, and the modified flow field is recalculated. Radial Basis Functions (RBFs) are used to accurately transfer structural displacements to the fluid mesh and ensure smooth, high-quality mesh deformation. Since the fluid and solid meshes typically have non-matching nodes at the interface, RBFs play a critical role in interpolating data across these meshes without loss of accuracy. Their ability to handle large deformations and maintain stability makes them essential for precise coupling in complex geometries. This loop continues until convergence is achieved by the end of the time step. Approximately 100 iterations were required per time step to achieve this convergence.

For the shape changes in the fluid domain cells resulting from the deformation of the solid due to its elasticity, OpenFOAM's dynamic mesh solver was used. This solver calculates the displacement of the corner coordinates of the cells in the direction of elastic deformation, while maintaining the existing number and layout of cells.

3. Results and Discussion

Solutions were obtained for three different angles of attack using the methodology provided. Initially, solutions were obtained assuming the plate is rigid, and the flow solver was validated against experimental data from the literature. Then, elastic solid-fluid interaction-based numerical solutions were obtained and compared with the rigid plate results.

Table 1: Fluid (air) properties

Density (ρ_f)	$1.225\ kg\ m^{-3}$
Dynamic viscosity (μ_f)	$1.802 \times 10^{-5}\ kg\ m^{-1}\ s^{-1}$

Table 2: Structure (rubber) properties

Density (ρ_s)	$1000\ kg\ m^{-3}$
Young (Elasticity) Modulus (E)	$50\ MPa$
Poisson ratio (v_s)	0.475

3.1 Simulation Setup and Parameters

Air was chosen as the fluid in the simulations, and its properties are given in Table 1. To observe significant solid deformations, rubber was selected as the solid material, and its mechanical properties are provided in Table 2. Rubber has its use in engineering applications such as morphing wings, inflatable aerodynamic decelerators, and flexible surfaces due to its high deformability and smooth aerodynamic behavior.

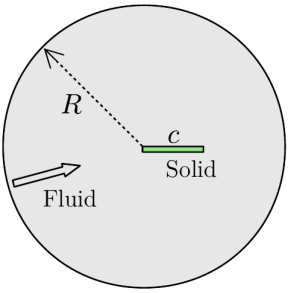

Figure 3: Schematic view of the solution domain

For all simulations, the plate's chord length was taken asc=0.16 m. The thickness of the plate was determined to be 2.5% of the chord length. The leading edge of the plate was placed exactly at the global origin. To ensure that the flow around the plate is not affected by the far-field boundary conditions, the radius of the flow domain was set to 100 times the chord length of the plate, R=100c (Figure 3).

The free-stream velocity was set to $U_\infty = 14.4\, m/s$, which results in a chord-based Reynolds number of $Re = 154{,}600$. All solutions were run for 4 seconds, allowing the flow field and solid deformation to stabilize. All time-averaged values were computed after the flow conditions had reached a steady state.

3.2 Flow Validation for the Rigid Plate

Before obtaining any fluid-structure interaction solutions, a simulation was performed on a completely rigid plate to test the accuracy of the flow solution. The obtained results were compared with experimental data from the literature. The reference study by Fage and Johansen (Fage & Johansen, 1927) reporting pressure coefficient distributions on a flat plate was used as the benchmark. To allow a direct comparison, the same Reynolds number used in the reference study was simulated. The results are presented in Figure 4, where the pressure coefficient c_p is defined as $c_p = p/(\frac{1}{2}\rho {U_\infty}^2)$, and the freestream pressure is $p_\infty = 0$.

The pressure distribution on the lower surface was predicted with high accuracy for all angles of attack, as flow separation does not occur here. A slight deviation can be observed at $\alpha = 6^o$, but this difference mainly occurs near the leading and trailing edges. On the other hand, the pressure distribution on the upper surface deviates more from the measurements. As the angle of attack increases, the reverse pressure gradient on the upper surface becomes stronger, and the separation point moves towards the leading edge, enhancing the separation effect. From the experimental data, it is evident that for $\alpha = 15^o$ and higher, the pressure distribution on the upper surface remains constant along the surface, indicating complete separation at the leading edge. Despite this separation, numerical and experimental results are relatively close for $\alpha = 15^o$ and beyond, with the most significant mismatch occurring at the trailing edge. The reference study did not specify the plate thickness; however, it is hypothesized that the plate used in the reference study was thinner, and the observed differences are likely due to the plate thickness. The pressure coefficient distribution is one of the most informative parameters regarding the accuracy of a flow solver. Obtaining results consistent with experimental reference data demonstrates that the current flow solver is adequate.

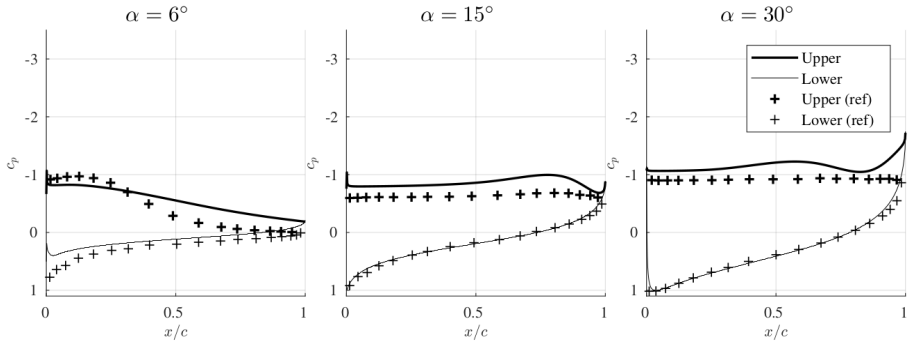

Figure 4: Pressure coefficient distribution at different angles of attack on a rigid plate. Ref: (Fage & Johansen, 1927)

3.3 Elastic Plate Solutions and Comparison with Rigid Plate

In this section, the aeroelastic model was activated, and the plate was allowed to deform freely in the cantilever beam configuration from the trailing edge. After a 4-second simulation, the average velocity and flow lines obtained are shown in Figure 5. The solutions obtained for the rigid plate show an increasingly stronger separation region with increasing angle of attack. At , this separation region is relatively narrow, but for higher angles of attack, it grows significantly, creating a larger separation region. Especially for and beyond, complete flow separation from the leading edge is evident. In the elastic plate solutions, the pressure distribution behaves like a vertically distributed positive load, causing upward deformation of the plate, which leads to significant changes in the separation region.

At the lowest angle of attack (), the flow separation region and circulation in this region became visible. As the angle of attack increases, the amount of displacement on the plate also increases. After elastic deformation, the separation-induced circulation region extends downstream, growing larger. At the highest angle of attack (), a secondary circulation region formed near the trailing edge. This region is expected to increase the drag due to pressure effects, thus negatively affecting the drag coefficient. In addition to the qualitative analysis of plate deformation, vertical displacement amounts were quantitatively evaluated and plotted in Figure 6. Here, is defined as the vertical displacement calculated along the horizontal axis (i.e.), non-dimensionalized by the plate length. As observed in Figure 5, the largest displacement occurs at the leading edge (). For , a 5% displacement at the leading edge occurred, while at and , this value reached 8.5% and 13%, respectively.

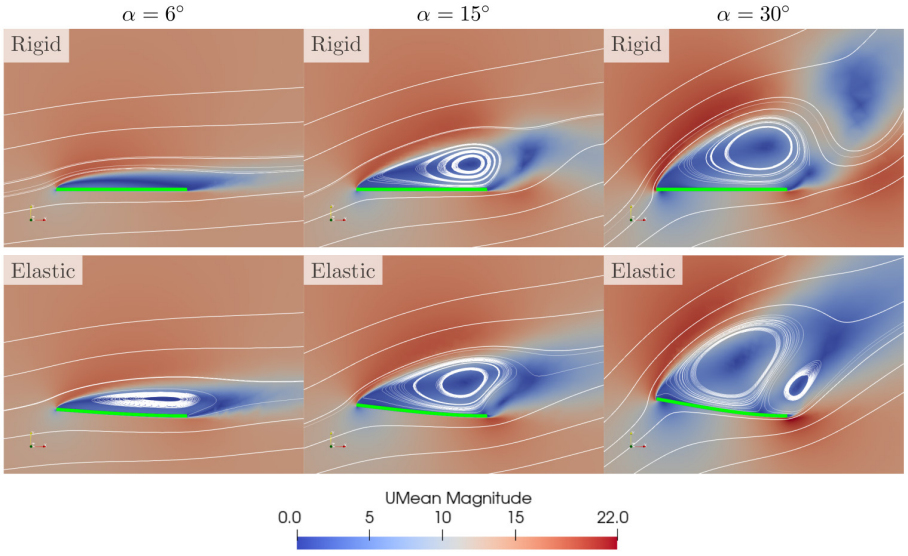

Figure 5: Average velocity contours and streamlines at different angles of attack for the rigid and elastic plates (velocity units: m/s).

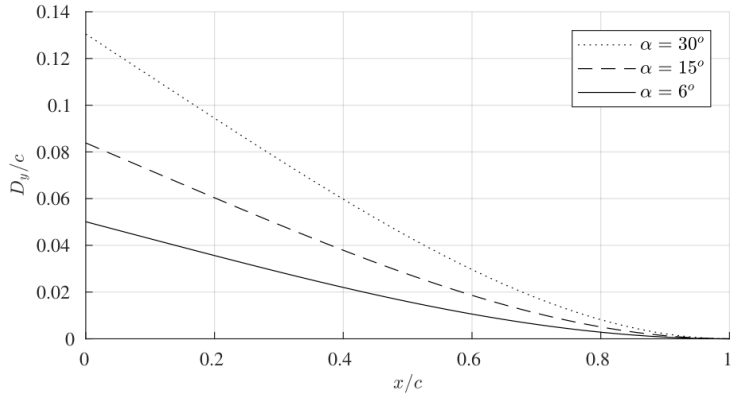

Figure 6: Normalized vertical displacement distributions obtained from aeroelastic simulations at different angles of attack

It is expected that the pressure distribution, which is a key factor in generating aerodynamic forces, will differ on the elastically deformed plate. As observed from the displacement ratios in Figure 6, this deformation leads to an additional effective angle of attack of approximately 4°, 6° and 9.5° at angles of attack α=6°, α=15° and α=30°, respectively. The change in the pressure distribution caused by this angle difference is shown in Figure 7. Since the displacement is non-linear and parabolic, this additional angle effect should be considered a rough estimate. At α=6°, suction loss was observed on the upper surface and pressure increase on the lower surface, from the leading edge to the middle of the plate. Considering that the leading edge moves upwards (increasing angle of attack), this result is as expected. In the rear half of the plate, the opposite behavior was observed. At α=15°, a similar behavior was observed, but the difference on the upper surface was less pronounced due to already strong flow separation and negligible additional deformation. At α=30°, a similar behavior was observed on the lower surface with minimal changes. In this case, the displacement on the upper surface was large enough to significantly affect the flow, causing noticeable pressure differences, especially near the trailing edge.

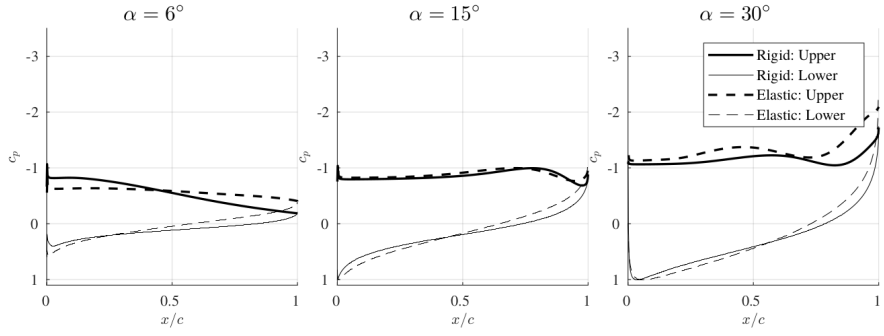

Figure 7: Comparison of the pressure coefficient distribution along rigid and elastic plates at different angles of attack

3.4 Comparison of Lift and Drag Coefficients

The lift and drag coefficients calculated for elastic and rigid plates at different angles of attack are given in Figure 8, where the force coefficient is $C_F=F/(1/2\ \rho U_\infty{}^2 c)$. At α=6°, the lift coefficient was calculated as 0.66, which matches the value obtained from thin airfoil theory ($C_L=2\pi\alpha$). As expected, at higher angles of attack, the calculated lift coefficient deviates from the theoretical value, as the flow at low angles of attack resembles inviscid and non-separated flow, which is the foundation of thin airfoil theory, while this is not the case at higher angles of attack.

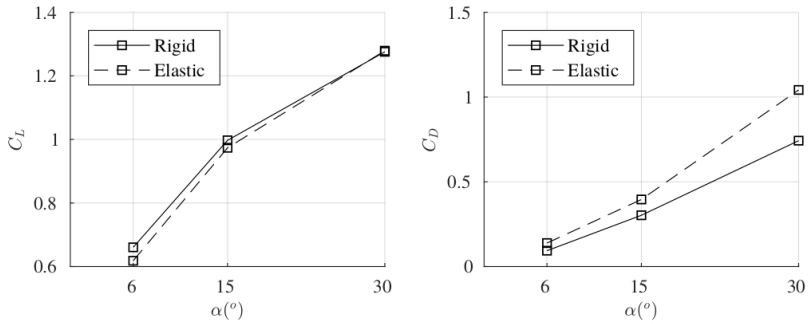

Figure 8: Variation of lift (left) and drag (right) coefficients for rigid and elastic plates at different angles of attack

Atα= 6°, elastic deformation resulted in a 6.4% loss in lift (Table 3). As the angle of attack increases, although elastic deformation also increases, its negative effect on lift becomes proportionally smaller. At α=30° , the lift force between elastic and rigid solutions becomes nearly identical. This is attributed to the large pressure drop near the upper surface, as seen in Figure 7. The drag coefficient increases as expected with higher angles of attack. The elastic deformation causes an approximately 48% increase in drag at ,α=6°, which decreases to 31% at α=15° and rises again to 40% at α=30°. As mentioned earlier, the upward deformation of the leading edge resembles the effect of increased angle of attack, and the pressure-induced drag component, which is already dominant due to strong flow separation, is more influenced by elastic effects. Overall, elastic deformation has a more negative impact on drag than on lift.

Table 3: Comparison of lift and drag coefficients for elastic and rigid plates at different angles of attack (*el:* elastic, *rl:* rigid)

Angle of attack, α	Lift difference, $C_L{}^{el}/C_L{}^{ri}$ 1	Drag difference, $C_D{}^{el}/C_D{}^{ri}$ 1
6^o	-6.4%	47.9%
15^o	-2.4%	30.8%
30^o	0.3%	40.3%

4. Conclusion

In this study, the effects of aeroelasticity and fluid-structure interactions (FSI) (which are often neglected in conventional aerodynamic simulations) have been systematically investigated with a focus on their influence on aerodynamic loads. A strongly coupled FSI framework was established using open-source finite volume solvers for both the fluid and structural domains, enabling direct feedback between aerodynamic forces and structural deformation. The flat plate in cantilever configuration was intentionally selected as a simplified geometry to isolate and clearly observe the fundamental effects of elasticity on flow behavior and force generation.

The results reveal that even in this idealized and relatively low-Reynolds-number configuration, structural deformation significantly alters the surface pressure distribution. These changes directly impact lift and drag characteristics, emphasizing the necessity of accounting for aeroelastic effects, especially in cases involving flexible structures. The numerical findings show a consistent degradation in aerodynamic performance due to elasticity, with up to 6% reduction in lift and as much as 47% increase in drag compared to the rigid-body assumption. This outcome suggests that structural flexibility, if not modeled, could lead to substantial underestimation of parasitic drag and overestimation of aerodynamic efficiency.

Moreover, simulations conducted at three angles of attack (6^o,15^o, and,30^o) demonstrate a clear trend: as the angle of attack increases, the relative impact of structural flexibility on lift decreases, potentially due to flow separation effects dominating lift behavior at high incidence. In contrast, drag remains significantly affected at all tested angles, indicating that pressure-induced deformation amplifies form drag regardless of angle. This highlights that, for the current configuration, the adverse effect of elasticity on drag is more dominant and potentially more critical in performance predictions.

5. References

Ayaz, A., & Memon, I. R. (2022). Comparative Study of Aeroelastic Response of Flat Plate Using Frequency & Time Domain Methods. *Proceedings of 2022 19th International Bhurban Conference on Applied Sciences and Technology, IBCAST 2022* 108–115. Doi: https://doi.org/10.1109/IBCAST54850.2022.9990296

Badshah, M., Badshah, S., & Jan, S. (2020). Comparison of computational fluid dynamics and fluid structure interaction models for the performance prediction of tidal current turbines. *Journal of Ocean Engineering and Science*, *5*(2), 164–172. Doi: https://doi.org/10.1016/j.joes.2019.10.001

Chimakurthi, S., Tang, J., Palacios, R., Cesnik, C., & Shyy, W. (2008, April 7). *Computational Aeroelasticity Framework for Analyzing Flapping Wing Micro Air Vehicles*. 49th AIAA/ASME/ASCE/AHS/ASC Structures, Schaumburg, IL. Doi: https://doi.org/10.2514/6.2008-1814

Chourdakis, G., Davis, K., Rodenberg, B., Schulte, M., Simonis, F., Uekermann, B., Abrams, G., Bungartz, H.-J., Cheung Yau, L., Desai, I., Eder, K., Hertrich, R., Lindner, F., Rusch, A., Sashko, D., Schneider, D., Totounferoush, A., Volland, D., Vollmer, P., & Koseomur, O. Z. (2022). preCICE v2: A sustainable and user-friendly coupling library. *Open Research Europe*, 2, 51. Doi:

https://doi.org/10.12688/openreseurope.14445.2

Chourdakis, G., Schneider, D., & Uekermann, B. (2023). OpenFOAM-preCICE: Coupling OpenFOAM with External Solvers for Multi-Physics Simulations. *OpenFOAM® Journal*, *3*, 1–25.Doi: https://doi.org/10.51560/ofj.v3.88

Fage, A., & Johansen, F. C. (1927). On the flow of air behind an inclined flat plate of infinite span. *Proceedings of the Royal Society of London. Series A, Containing Papers of a Mathematical and Physical Character*, 116(773), 170–197. Doi: https://doi.org/10.1098/rspa.1927.0130

Fagley, C., Seidel, J., & McLaughlin, T. (2015). Aeroelastic response of a finite span NACA 0018 wing part 2: Computational simulations. *53rd AIAA Aerospace Sciences Meeting*. https://doi.org/10.2514/6.2015-0250

Geuzaine, P., Brown, G., Harris, C., & Farhat, C. (2003). Aeroelastic Dynamic Analysis of a Full F-16 Configuration for Various Flight Conditions. *AIAA Journal*, *41*(3), 363–371. https://doi.org/10.2514/2.1975

Grifò, M., Da Ronch, A., & Benedetti, I. (2023). A computational aeroelastic framework based on high-order structural models and high-fidelity aerodynamics. *Aerospace Science and Technology*, *132*, 108069. https://doi.org/10.1016/j.ast.2022.108069

Grinderslev, C., González Horcas, S., & Sørensen, N. N. (2021). Fluid–structure interaction simulations of a wind turbine rotor in complex flows, validated through field experiments. *Wind Energy*, *24*(12), 1426–1442. https://doi.org/10.1002/we.2639

Heinz, J. C., Sørensen, N. N., & Zahle, F. (2016). Fluid–structure interaction computations for geometrically resolved rotor simulations using CFD. *Wind Energy*, *19*(12), 2205–2221. https://doi.org/10.1002/we.1976

Issa, R. I. (1986). Solution of the implicitly discretised fluid flow equations by operator-splitting. *Journal of Computational Physics*, *62*(1), 40–65. https://doi.org/10.1016/0021-9991(86)90099-9

Maza, M. S., Preidikman, S., & Flores, F. G. (2023). A cost-effective algorithm for the co-simulation of unsteady and non-linear aeroelastic phenomena. *Journal of Fluids and Structures*, *118*, 103838. https://doi.org/10.1016/j.jfluidstructs.2023.103838

Menter, F. R., Kuntz, M., & Langtry, R. (2003). Ten Years of Industrial Experience with the SST Turbulence Model Turbulence heat and mass transfer. *Cfd.Spbstu.Ru*, *4*(July 2014), 625–632.

Nawafleh, A., Xing, T., Durgesh, V., & Padilla, R. (2022). Fluid-Structure Interaction Simulation of a Flapping Flag in a Laminar Jet. *SSRN Electronic Journal*. https://doi.org/10.2139/ssrn.4187523

Neumann, J., Nitzsche, J., & Voss, R. (2008). Aeroelastic Analysis by Coupled Non-Linear Time Domain Simulation. *AVT-154 Specialists Meeting on Advanced Methods in Aeroelasticity*, 1–21.

Patankar, S. V., & Spalding, D. B. (1983). A Calculation Procedure for Heat, Mass and Momentum Transfer in Three-Dimensional Parabolic Flows. *Numerical Prediction of Flow, Heat Transfer, Turbulence and Combustion*, 54–73. https://doi.org/10.1016/b978-0-08-

030937-8.50013-1

Piperno, S. (1997). Explicit/implicit fluid/structure staggered procedures with a structural predictor and fluid subcycling for 2D inviscid aeroelastic simulations. *International Journal for Numerical Methods in Fluids*, *25*(10), 1207–1226. https://doi.org/10.1002/(SICI)1097-0363(19971130)25:10%3C1207::AID-FLD616%3E3.0.CO;2-R

Schuster, D. M., Liu, D. D., & Huttsell, L. J. (2003). Computational Aeroelasticity: Success, Progress, Challenge. *Journal of Aircraft*, *40*(5), 843–856. https://doi.org/10.2514/2.6875

Sheta, E. F., Harrand, V. J., Thompson, D. E., & Strganac, T. W. (2002). Computational and experimental investigation of limit cycle oscillations of nonlinear aeroelastic systems. *Journal of Aircraft*, *39*(1), 133–141. https://doi.org/10.2514/2.2907

Silva, W., & Bartels, R. (2002, April 22). Development of Reduced-Order Models for Aeroelastic Analysis and Flutter Prediction Using the CFL3Dv6.0 Code. *43rd AIAA/ASME/ASCE/AHS/ASC Structures, Structural Dynamics, and Materials Conference*. 43rd AIAA/ASME/ASCE/AHS/ASC Structures, Structural Dynamics, and Materials Conference, Denver, Colorado. https://doi.org/10.2514/6.2002-1596

Weller, H. G., Tabor, G., Jasak, H., & Fureby, C. (1998). A tensorial approach to computational continuum mechanics using object-oriented techniques. *Computers in Physics*, *12*(6), 620. https://doi.org/10.1063/1.168744

Wood, J. N., Breuer, M., & De Nayer, G. (2020). Experimental investigations on the dynamic behavior of a 2-DOF airfoil in the transitional Re number regime based on digital-image correlation measurements. *Journal of Fluids and Structures*, *96*. https://doi.org/10.1016/j.jfluidstructs.2020.103052